

Probing molecular environment through photoemission delays

S. Biswas^{1,2}, B. Förg^{1,2}, L. Ortmann³, J. Schötz^{1,2}, W. Schweinberger^{1,4},
T. Zimmerman⁵, L.-W. Pi³, D. Baykusheva⁶, H. A. Masood⁴, I. Lontos⁴, A. M.
Kamal⁴, N. G. Kling¹, A. F. Alharbi⁷, M. Alharbi⁴, A. M. Azzeer⁴, G. Hartmann^{8,9}
H. J. Wörner⁶, A. S. Landsman^{3,10,*}, M. F. Kling^{1,2,*}

¹Physics Department, Ludwig-Maximilians-Universität Munich, D-85748 Garching, Germany

²Max Planck Institute of Quantum Optics, D-85748 Garching, Germany

³Max Planck Institute for the Physics of Complex Systems, D-01187 Dresden, Germany

⁴Attosecond Science Laboratory, Physics and Astronomy Department, King Saud University, Riyadh 11451, Saudi Arabia

⁵Department of Mathematics, ETH Zurich, 8092 Zurich, Switzerland

⁶Laboratory of Physical Chemistry, ETH Zurich, 8093 Zurich, Switzerland

⁷King Abdulaziz City for Science and Technology (KACST), Riyadh 11442, Saudi Arabia

⁸Deutsches Elektronen-Synchrotron (DESY), D-22607 Hamburg, Germany

⁹Institut für Physik, University of Kassel, D-34132 Kassel, Germany

¹⁰Department of Physics, The Ohio State University, Columbus, Ohio 43210, USA

*Emails: landsman@pks.mpg.de, matthias.kling@lmu.de

Attosecond chronoscopy with ultrashort laser pulses has revealed small but measurable delays in photoionization, characterized by the ejection of an electron upon absorption of a single photon. Ionization delay measurements in atomic targets provide a wealth of information about the timing of the photoelectric effect, resonances, electron correlations and transport. The extension of this approach to molecules, however, presents great challenges, such as identifying correct ionization channels and the effect of the anisotropic molecular landscape on the measured delays. Here, we measure ionization delays from ethyl iodide around a giant dipole resonance. By using the theoretical value for the iodine atom as a reference, we disentangle the contribution from the functional ethyl group, which is responsible for the characteristic chemical reactivity of a molecule. We find significant additional delay caused by the presence of a functional group, which encodes the effect of the molecular potential on the departing electron. Such information is inaccessible to the conventional approach of measuring photoionization cross-sections. The results establish ionization delay measurements as a valuable tool in investigating electronic properties of molecules.

The advent of high-intensity ultra-short lasers, awarded with the Nobel prize in physics in 2018, enabled the reconstruction of fundamental processes inside atoms and molecules on the attosecond (as) time-scale¹. One such process is Einstein's photoelectric effect, characterized by electron emission upon absorption of a single photon. It proved the discrete nature of light and was instrumental to the subsequent development of quantum mechanics. The target-specific delay of this photoemission process is given by the Eisenbud-Wigner-Smith (EWS) delay, which relates photoemission to a half-scattering event, and can be calculated from the energy derivative of the phase of the ionized electron wavepacket². This time delay provides important information on the electronic structure of matter, including electron correlations and the details of the atomic or molecular potential in which electrons move. These can help us develop and validate theoretical models describing electronic excitations in molecules.

Attosecond time delays in photoemission have been studied extensively in the past decade using streaking³⁻⁶ or RABBITT⁷⁻¹² experiments, which combine a weak isolated attosecond pulse (IAP) or pulse train, respectively, performing single photon ionization, with a probing infrared laser pulse. Such experiments³⁻¹¹ and the wealth of theoretical studies, they inspired^{13,14}, have been mainly confined to atomic targets. Recently, photoionization delays have been measured in simple molecules^{7,11,15}. However, the physical interpretation of such experiments is extremely challenging for the following reasons.

First, it is extremely difficult to isolate a specific ionization channel in a molecule due to spectral congestion resulting from closely spaced energy levels^{9,10,14}. Combined with the relatively broad bandwidth of an IAP, this makes it often impossible to assign correct initial electronic states based on final electron energies, even for simplest diatomic molecules¹¹. Second, the ionization process can be viewed as being comprised of two highly complex steps: the initial ionization of the electron, followed by subsequent propagation in the molecular potential. Since the electronic states involved in the ionization process are unique to that particular molecule, there is normally no reference to disentangle these two steps and separate the contribution of the molecular potential in which the ionized electron wavepacket moves.

Here, we overcome these challenges by measuring attosecond ionization delays in a polyatomic molecule, ethyl iodide, around a giant dipole resonance. Unlike other resonances, being an inner shell characteristic, the giant dipole resonance is known to remain largely unaffected when an atom becomes part of a larger molecule: "If a 'giant resonance' is present in an atom, then we expect to find it, with perhaps slight variations of the profile shape, in molecules containing this atom, or indeed in the condensed phase. This persistence of the resonance is unique amongst excited atomic states, and contrasts sharply with Rydberg behaviour. It provides experimental confirmation that the effect originates deep inside the atom..." (Quote from page 3 of Ref. ¹⁶). This is illustrated for the 4d resonance in Fig. 1(c), where photoionization cross sections (the absolute values are subject to discussion in the literature¹⁷) for atomic and molecular iodine, and iodine containing molecule are shown. In addition, the lifetime of a giant resonance is several orders of magnitude shorter than typical autoionizing states ¹⁶. Hence, any significant measured delays will be largely incurred during the propagation step, thereby providing information on the molecular potential landscape experienced by the escaping electron wavepacket. Hence, in the case of a giant dipole resonance in the iodine-containing molecule, the iodine atom therefore provides a natural reference, which allows us to both identify the initial electron localization, deep inside the iodine atom, and subsequent ionization pathway, and disentangle the two steps of the ionization process. The first step refers to a dipole $4d \rightarrow f$ transition, with the corresponding giant resonance being very similar in iodine and ethyl iodide. The second step refers to propagation of the freed electron in the atomic and molecular potential, respectively. Being able to disentangle the two steps of the ionization process therefore presents a unique opportunity to measure the effect of the molecular potential, in this case introduced by the ethyl group, on the propagation of an ionized electron wavepacket, initially localized around an iodine atom. We find that the addition of an ethyl group introduces an additional delay of up to around 38.0 ± 21.4 as, indicating a significant modification of the potential landscape observed by the escaping electron. Noteworthy, this occurs even though the ethyl group does not directly participate in the ionization process, with the hole being initially confined to the inner shells of the iodine atom, and without molecular orientation. Our study disentangles the effect of a functional group on ionization delays in a molecule, with possible implications for

the timing of electron transfer in chemical reactions. We note that the comparison of ionization cross sections between atomic and molecular species can contain information on the molecular environment during the ionization process, while time delay measurements, introduced here, provide information exclusively about the molecular environment as experienced by the liberated escaping electron during the propagation.

Results and discussion

The experimental approach, employing attosecond streaking spectroscopy¹, is illustrated in Fig. 1(a), and described in detail in the Methods section. In brief, IAPs in the extreme ultraviolet (XUV) regime at 80 eV and 93 eV with a bandwidth of 6.5 eV are generated from phase-stabilized few-cycle near-infrared (NIR) laser pulses of less than 5 fs duration at 750 nm central wavelength. The XUV and NIR pulses are focused with a variable pulse delay onto the target comprised of neon atoms and ethyl iodide molecules. Photoelectrons are generated by XUV ionization and propagate within the respective molecular or atomic potential, superimposed by the NIR laser field, which ponderomotively alters the electrons' momenta. The pulse-delay dependent momentum distributions of photoelectrons are detected with a time-of-flight (TOF) spectrometer.

As an example for the experimental results from streaking measurements (also see Supplementary Material (SI)), Fig. 2(a) shows a streaking spectrogram obtained with 93 eV photons, where two strong and one faint contributions can be discerned that oscillate with pulse delay. The faint contribution near 80 eV arises (see Fig. 2(f)) from valence emission from ethyl iodide. Analysis of the valence emission is not informative, since ionization can take place from a total of six orbitals within the bandwidth of the IAP¹⁸. Due to the multi-orbital contributions, the photoelectron valence emission yields a broad spectral feature with no distinct spectral peak. In contrast, the trace around 71.5 eV stems from photoionization from the neon 2p subshell. The large photoionization cross section for neon atoms¹⁹ permits clear identification of the neon 2p peak and a good signal-to-background ratio with respect to the partially overlapping ethyl iodide valence electrons. The contribution at around 37.5 eV in the photoelectron spectrum is attributed to the emission from the 4d subshell of iodine in ethyl iodide. A potential contribution from neon 2s in this energy region is negligible (cf. Fig. 2(f)). The obtained binding potential around 55.5 eV for the 4d emission band is in close agreement with literature values of 4d ionization from atomic iodine^{20,21}. In the experiments, the probed molecules experience NIR laser intensities around 10^{11-12} W cm⁻², for which laser-induced distortions of the molecule's electronic structure can be safely neglected. Note that all recorded NIR-induced above-threshold ionization (ATI) contributions are below 16 eV, not overlapping with the interrogated bands shown in Fig. 2(a).

To extract streaking traces from the measured spectrograms for different bands we utilize machine learning (ML). For the training of the ML approach (see Methods for details), the initial parameters are kept as randomized as possible: e.g. up to ten streaking features are considered with random initial parameters like positions, widths, intensities and streaking frequencies, within reasonable bounds, followed by addition of random jitter. The desired outputs of the algorithm are the streaking traces of each band in combination with their intensity and width. This trained ML algorithm is applied to the experimental streaking spectrogram to simultaneously extract streaking traces for all discernible bands. To complement this approach, another established model, namely nonnegative least square

optimization (NNLS)²² (see Methods for details) is also applied to extract streaking traces, resulting in almost identical outputs with that of the ML approach. These approaches treat the image as a whole and identify streaking patterns not only at the current delay step of the scan but by a combination of multiple previous and upcoming electron spectra. This makes the algorithm less sensitive to noise and allows to extract streaking traces from low intensity signals in a more reliable way. As an example, the extracted streaking traces are shown in Fig. 2(b) for the neon 2p and ethyl iodide 4d emission.

To evaluate the relative streaking time delay of the ethyl iodide 4d emission, we calculate the phase delay relative to the neon 2p emission by transforming these retrieved streaking traces into the Fourier domain (see details in the Methods and SI). The Fourier-filtered data in the temporal domain, where components outside the incident NIR frequency range are omitted, is shown in Fig. 2 (b). From the spectral phases of the neon and ethyl iodide streaking traces, we calculate the relative streaking phase delay according to

$$\Delta t_s(\omega) = \frac{\phi^{I-4d}(\omega) - \phi^{Ne-2p}(\omega)}{\omega}, \quad (1)$$

where $\phi(\omega)$ represents the spectral phase of the ethyl iodide and neon streaking traces and ω describes the laser angular frequency. Using the spectral intensity of the neon streaking trace $I_{Ne}(\omega)$ as a weighting function, the relative streaking time delay Δt_s for each measurement is calculated by averaging over the streaking phase delay values:

$$\Delta t_s = \frac{\sum_{\omega} I_{Ne}(\omega) \cdot \Delta t_s(\omega)}{\sum_{\omega} I_{Ne}(\omega)}. \quad (2)$$

The obtained results for different measurements at 80 eV and 93 eV are depicted in Fig. 2 (d) and (e), respectively, as a function of NIR intensity. It is evident that the delays are insensitive to the NIR intensity within the covered range, which designates insignificant polarization effects and distortions of the molecule. This also indicates the robustness of the results against partial contamination with ATI signals, especially at 80 eV. Average mean values and standard deviations of relative streaking delays are obtained from this data with 51.8 ± 21.2 as (80 eV) and 18.5 ± 4.3 as (93 eV), respectively. Given the different orders of magnitude between streaking delay and the period of the NIR field, the small streaking delay is only discernible upon close inspection of the streaking traces, as illustrated in Fig. 2(c).

To contest the above approaches, which we introduced here for extracting streaking traces, we also retrieved the streaking curves by calculating the central energy after fitting Gaussian functions (GF) to the photoelectron spectrum at each delay step for individual bands. The resultant relative streaking delay value (see Fig. 3) at 80 eV, after following the same Fourier analysis described above, comes out to be nearly same but with much larger standard deviation (50.8 ± 35.8 as), whereas for 93 eV the value (17.4 ± 5.6 as) remains very similar to the ML approach. This clearly indicates the consistency and success of the ML analysis, especially for the noisier data at 80 eV. Both the analysis indicate the spectral broadening of the ethyl iodide 4d-emission structure, which can be attributed to the spin-orbit splitting of the 4d photoelectron band, with two components ($4d_{5/2}$ and $4d_{3/2}$) separated by 1.7 eV ²³, which are not resolved because of the bandwidth of the attosecond pulse. However we note that the relative photoionization delays between photoemission from the two spin-orbit components of iodine 4d are expected to be similarly small as those measured in the case of xenon 4d with $(-4 \pm 4.1) \text{ as}$ ²⁴.

In Fig. 3(a), we compare the experimental streaking delays to theoretical predictions using the Classical Wigner Propagation (CWP) method^{11,25}, where the electronic structures of the ground states of ethyl iodide and neon are calculated either based on frozen-core Hartree-Fock (HF) or configuration interaction singles (CIS) formalisms. Here we have added an experimental data point at 105 eV, which was extracted from Ossiander *et al.*²⁶. In the first step of CWP, a bound electron is ionized into the continuum following the absorption of a single photon from the weak attosecond XUV pump pulse. This process is well-described within first-order perturbation theory. In the second step, the wave function of the photoionized electron is propagated in the presence of the NIR laser field by a classical Wigner propagator within the dipole approximation (for a detailed description of CWP formalism, see^{11,25}). From the simulated spectrograms, the relative streaking phase delay and subsequently the relative streaking delay for ethyl iodide photoemission are calculated following the same analysis scheme described above for the experimental data. As this approach incorporates effects induced by Coulomb-laser coupling (CLC)²⁷⁻²⁹, illustrated as inset to Fig. 3(a), the simulated results are directly comparable to experimental streaking delay values. The calculations yield nearly overlapping values from HF and CIS, indicating negligible contributions of excited states. Both HF and CIS simulations agree very well with experimental measurements at higher energies and are well within standard deviation for the lowest energy measurement at 80 eV.

In addition to the CWP calculations, we use an independent theoretical approach, based on molecular quantum scattering theory (QST), described in detail in Ref. ³⁰. According to this approach, the photoionization delay as a function of electron energy and emission direction in the molecular frame is defined as the energy derivative of the phase associated with the photoionization transition matrix element. The latter is calculated using the molecular orbitals of the neutral molecule obtained from HF calculations and electronic continuum wave functions obtained through the variational Schwinger method. Hence, the QST approach directly provides the EWS delay, which can be compared to experiment after the CLC term is added to the latter. To describe the full dynamics in the laboratory frame, the calculated delays were isotropically averaged over all molecular orientations. For better comparison with experimental findings, the results from the full QST are additionally averaged over all photoelectron emission directions, whereby the range is determined by the detector's acceptance angle in the experiment (a cone with 45° full opening angle around the NIR laser polarization).

The EWS delays predicted by QST and CWP calculations for ethyl iodide are compared to the experimental data in Fig. 3(b). For experimental data and the CWP simulations, the CLC contribution, as shown in Fig. 3(a) inset, evaluated according to Ref. ¹⁴, is subtracted from the relative streaking delay. The CLC contribution is due to the long-range Coulomb interaction between the departing electron and the positively charged parent ion, and is therefore nearly identical across all atoms and molecules, for a given electron energy. The EWS delays for neon 2p, calculated using the CIS formalism and added to the relative streaking values along with the CLC subtraction to obtain the absolute EWS delay, are shown for comparison, and yield nearly insignificant contributions over the studied energy range. In general, within the investigated energy region, both theoretical models predict positive EWS delays thus matching the conclusions of the calculations in Refs. ³¹ and ²⁴, and a universal increase of EWS delays with decreasing photon energy, in accordance with the experimental findings

We find that both theories make very similar predictions at higher energies and disagree somewhat at lower energies, with the experimental data point at 80 eV falling closer to the CWP predictions compared to the other for EWS delays. At higher energies all the theoretical predictions match excellently with the experimental findings. The disagreement at lower energies can be understood by considering that accurate theoretical estimates become much more difficult at lower energies due to the increased influence of the short-range molecular potential, which is difficult to capture in all its complexity, particularly for polyatomic molecules. Although more difficult to measure experimentally and model theoretically, the lower energy data is most valuable as it contains a wealth of information, encoded in the EWS delay, about the short-range potential landscape. As can be seen from Fig. 3(b), this short-range potential leads to significant additional delay, of around 38.0 ± 21.4 as.

Generally, the rise in the EWS delay is expected for both shape and giant 4d-resonances. For giant resonances, intershell and intrashell interactions can influence the photoemission delay and this particular contribution was debated in prior theoretical works^{31,32}. In addition to the delay being due to the transient trapping of the electron wavefunction, such as observed in a shape resonance⁷, electron correlations can also play a significant role³¹. For instance, short-range electron-electron repulsion can offset the negative CLC term (shown in Fig. 3(a) inset).

In contrast to the valence electron emission studied so far in most of the previous works^{7,11,15}, the giant dipole resonance in ethyl iodide is due to ionization from an inner 4d shell of the constituent iodine atom. As such, the ionized electron wavepacket is spatially localized near the iodine end of the molecule at the time of ionization and the ionization process is barely affected by the molecular environment. This is well reflected in the comparison between the phase space representations of the initial giant resonance ionization steps for atomic iodine and ethyl iodide, as shown in Fig. 4(a - d). It can be seen that the first ionization step is very similar for the atom and the molecule. This implies that the escaping electron can probe the molecular landscape introduced by the remaining molecular fragment (i.e. the ethyl group, see Fig. 1(a)) as it traverses through it. The comparison of the experimentally measured streaking delay and EWS delay for ethyl iodide with the theoretical values for ethyl iodide and atomic iodine, presented in Figs. 3(a) and 3(b), expresses the molecular influence. We note that, experimentally, atomic iodine would need to be obtained from a molecular precursor, a process that is not 100% efficient and causes overlap between atomic and molecular signals. We thus rely here on theoretical data for atomic iodine using the well tested CWP formalism^{11,25}. Since the initial ionization step, and its contribution to the streaking or EWS delay, is virtually the same (resulting from ionization of the inner shell of iodine), the difference between ethyl iodide and atomic iodine is due to the subsequent propagation step of the electron within the molecular potential. This can be identified exclusively as the impact of the molecular potential on the departing electron wavepacket. Fig. 3(a) and (b) clearly show an overall shift of the streaking delay as well as EWS delay in the case of ethyl iodide compared to iodine. At lowest energy, the EWS delay shift is around 38.0 ± 21.4 as, which decreases with increasing photon energy. The theoretical estimates also show an overall shift, however, with decreased magnitude at lowest photon energy. The decrease in shift with increasing photon energy is expected from the fact that the higher energy XUV generates higher kinetic energy photoelectrons, which spend less time in the molecular environment compared to the lower kinetic energy photoelectrons. As a result, the lower energy electrons are influenced more by the molecular potential, which is manifested as larger delay difference compared to the atomic iodine.

The influence of the molecular environment in other, related systems was studied theoretically, as shown in Fig. 4(e). The data has been calculated within the classical Wigner-CIS formalism showing the effect of a variable ligand attached to the iodine atom. For ethyl iodide the distribution is nearly isotropic. As the ligand mass increases, however, the angular dependent photoemission delays are less flat. For an iodine atom as a reference, we expect an isotropic distribution, which is actually still seen, much surprisingly, for ethyl iodide. For the other two molecules the delay is minimal for normal electron ejection whereas it increases as the photoionized electron escapes in the direction of the ligand or opposite to it. This difference can be attributed to the influence of the molecular environment. Here, we also show the angle integrated delay value for these molecules (dashed horizontal lines), which manifest an increase of overall delay with the size of the ligand, enabling to observe the molecular influence even without angular-resolved measurements.

Conclusions

In conclusion, we find that the EWS delay of an escaping electron wavepacket around a giant dipole resonance increases significantly due to the presence of a functional group. The experimentally measured EWS delay of around 67.5 ± 21.2 as, which is about 38.0 ± 21.4 as larger compared to the case without functional group, at lower energies, is particularly significant when one considers that, out of all the halogens, the iodine has the lowest electronegativity. As a result, the attached alkyl group is close to neutral, suggesting that even a neutral ligand can measurably modify the potential landscape seen by the departing electron. Therefore, the EWS delay provides sensitive information about the role of a functional group in a molecule, which cannot be obtained by the usual technique of measuring ionization cross sections.

The angular-resolved simulations for other iodide-containing molecules suggest that the delay correlates with the size of the attached group. These observations open up new perspectives for angle-resolved EWS delay measurements in molecules to probe the potential landscape in three dimensions. Finally, since functional groups determine the characteristic chemical properties of a molecule, understanding their influence on ionization delays is crucial for the ultimate goal of steering chemical reactions using attosecond pulses³³. Given the complexity of the system, the agreement between theory and experiment, and thereby unleashing the exclusive role of molecular environment on the ultrafast ionization process contributes to the development of strong field molecular physics as well as other fields of physics and chemistry.

Acknowledgement

We acknowledge fruitful discussions with and support from F. Krausz. We are grateful for support from the King-Saud University in the framework of the MPQ-KSU-LMU collaboration. S.B. acknowledges support from the MULTIPLY fellowship program under Marie Skłodowska-Curie COFUND Action and the Alexander von Humboldt foundation. B.F. and J.S. acknowledge support from the Max Planck Society via the IMPRS-APS. M.F.K. is grateful for support from Max Planck Society and the DFG via KL-1439/11-1.

Data Availability

The data that support the findings of this study are available from the corresponding authors upon reasonable request.

Author contributions

S.B., B.F., and L.O. contributed equally to this work. S.B., B.F., J.S., W.S., H.A.M., I.L., A.M.K., N.G.K., A.F.A., M.A., A.M.A., and M.F.K. conducted the experiments. S.B. and B.F. did the data analysis. G.H. wrote the ML code and extracted streaking traces. L.O., T.Z, and A.S.L. did the CWP calculations. L.-W.P. performed TDLDA simulations. D.B. and H.J.W. did the QST calculations. S.B., B.F., L.O., T.Z., D.B., H.J.W., A.S.L., and M.F.K. wrote the manuscript, which was reviewed by all authors.

Competing Interests

The authors declare no competing financial interest.

Methods

Experimental Setup:

The laser setup and attosecond beamline at the Attosecond Science Laboratory of the King Saud University have been described elsewhere³⁴. Briefly, the pulses used in the experiment are delivered by a commercial laser system (FEMTOPOWER compact PRO HP/HR 3 kHz, Spectra Physics). The system delivers carrier envelope phase (CEP) stable 25 fs pulses with an energy of up to 800 μ J. The pulses are spectrally broadened in a hollow-core fiber filled with neon to a width of 300 nm centered at 750 nm, supporting sub-two cycle pulses. The pulses are subsequently compressed by a set of chirped mirrors. Finally, phase-stable few-cycle pulses of duration around 4.7 fs with 350 μ J at 3 kHz repetition rate are delivered to the experiment. In the attosecond beamline, XUV light is generated via high-harmonic generation (HHG), whereafter XUV and fundamental NIR beams are spatially separated with a concentric Zr-foil filter and the double mirror that focuses both beams onto the target. The coating of the inner mirror, which focuses the XUV beam, supports a bandwidth of 6.5 eV around different central photon energy selected in the cutoff region of the HHG spectrum. The XUV-NIR pulse delay can be adjusted with a piezo stage attached to the inner mirror. The target gases are delivered to the interaction volume through a thin nozzle. The gas mixture is prepared within an external bubbler system, where the neon gas goes into the ethyl iodide liquid through an input tube, and the neon-ethyl iodide mixture evaporates and is guided to the gas nozzle by an output tube. The ionized electrons are captured by a TOF spectrometer equipped with an electrostatic lens and microchannel plate detector at the end.

Retrieval of streaking delay:

To extract the streaking traces from the experimental streaking spectrograms total three approaches are adapted. First, out of a measured streaking spectrogram, the streaking curves for different bands (ethyl iodide (4d), neon (2p) and ethyl iodide (HOMO)) are extracted using machine learning based analysis. This involves extensive training of the algorithm with test data sets. The test data sets are created with parameters as general as possible involving multiple streaking features (up to ten) at random positions, with random widths, intensities and streaking frequencies. At each delay slice, a random jitter is added to all the previous parameters. The trained algorithm, which produces the output as the traces corresponding to each band in combination with their intensity and width, is applied to the experimental data. Different models were applied on this training data with almost identical results for the analysis of the experimental data. One of the models is to learn the transformation $X \rightarrow Y$ via a multi-layer neural network³⁵ with a drop rate for preventing overfitting³⁶. Second more established approach uses the assumptions, which were put into the training data as conditions in an optimization routine. This analysis takes way more calculation time but is not using the training data at all. It was realized by nonnegative least square optimization with a rather huge basis set of traces. In this NNLS-optimization²² the (L2-) regularization was achieved by Tikhonov matrix shaped as Identity scaled by a factor $\ll 1$. The NNLS algorithm is very similar to the one used in Ref. ³⁷. In essence, all these models and the applied training data sets are proven to be robust against the reconstruction of all streaking traces at once from an experimental streaking spectrogram.

In addition to the above analyses, as third approach, we employed manual analysis based on Gaussian curve fitting over the electron spectrum identify the streaking traces. Corresponding

to ethyl iodide 4d and neon 2p emissions, at each delay step, Gaussian functions are independently fitted to the photoemission yields within a limited energy range around the respective peak maxima. The central energies providing the best fits, define the streaking traces for the respective emission orbitals. For the neon streaking spectrogram, though it is marginally contaminated by ethyl iodide valence electron emission, the large photoionization cross section facilitates the ability to resolve the peak structure at any delay position. For 80 eV data (see Fig. S1 in SI), a similar situation also occurs for the ethyl iodide 4d emission peak, which is marginally contaminated by ATI electrons induced by the few-cycle laser field. However, using a reduced NIR intensity, and because of the large cross section at the iodine giant resonance, the peak structure remains clearly distinguishable throughout the full delay range.

To retrieve the streaking time delays, streaking traces are Fourier transformed (FT), following zero padding, into the spectral domain, which yields the spectral amplitude and phase (see SI). Since phase and time shift are inherently connected, the relative streaking phase delay $\Delta t_s(\omega)$ between the two emission lines is calculated according to

$$\Delta t_s(\omega) = \frac{\phi^{I-4d}(\omega) - \phi^{Ne-2p}(\omega)}{\omega}, \quad (\text{M1})$$

where $\phi^{I-4d}(\omega)$ and $\phi^{Ne-2p}(\omega)$, represent the spectral phases of ethyl iodide and neon streaking traces, respectively, while ω stands for the NIR laser angular frequency. The resulting relative streaking phase delay $\Delta t_s(\omega)$ is nearly a flat function of angular frequency (see in SI), for which the average or the relative streaking delay is calculated according to

$$\Delta t_s = \frac{\sum_{\omega} I_{Ne}(\omega) \cdot \Delta t_s(\omega)}{\sum_{\omega} I_{Ne}(\omega)}. \quad (\text{M2})$$

where the spectral intensity ($I_{Ne}(\omega)$) for neon is used for averaging. The method of calculating delay from the scattering phase is well established, previously used in e. g. Ref. ^{7,11} (see Ref. ¹⁴ and ¹³ for details).

Classical Wigner propagation method calculations:

The photoelectron in the Classical Wigner Propagation (CWP) method is described by the Wigner function, which is sampled by individual trajectories that are then propagated classically. The Wigner function itself is derived from the first-order perturbation theory wave function describing the single-photon ionization of the electron by the XUV field. This approximation is justified by relatively weak XUV pulses used in streaking experiments. The single-electron zeroth-order wave function is determined from the Dyson orbital corresponding to a chosen final ionic state. The interaction with the probe NIR field is then described non-perturbatively during the classical propagation. The detailed derivation of the method is presented in Ref. ²⁵ and further information can be found in the supplemental information of Ref. ¹¹. Here, we provide the specific parameters that were used to simulate streaking delays of the 4d orbital in ethyl iodide.

The peak intensity of the XUV pulse used in the calculations was $3.51 \times 10^{16} \text{ W cm}^{-2}$. The envelope was Gaussian shaped with a full width at half maximum (FWHM) of around 260 as. The NIR pulse had a wavelength of 750 nm, an intensity of $8 \times 10^{12} \text{ W cm}^{-2}$ and a Gaussian-shaped envelope with a FWHM of 7 fs. Even though the intensities of the pump and probe

pulses used in simulations do not exactly match with the experimental values, it is well known that streaking delays are insensitive to the XUV and NIR intensities⁵. Therefore, the results of the CWP simulations should be directly comparable with the experimental values.

The Dyson orbitals, given by the overlap of multi-electron wavefunctions of the neutral molecule and of an ion with a missing 4d electron, were computed using Superdyson³⁸. The neutral and ionized molecular wavefunctions were computed using the Hartree-Fock (HF) or CIS method (the latter allowing for ionization only from 4d orbitals) using a double-zeta 6-31G** or correlation-consistent triple-zeta (cc-TZVP) basis set, respectively. For the CIS, the ORMAS program from the quantum-chemistry package Gamess was used³⁹. The core electrons of iodine were described with a model core potential (MCP)^{40,41}. The electrostatic forces between the ionizing electron and the ion were computed from the one-particle density matrix derived from the HF or CIS wave function of the ion in the double-zeta 6-31G** basis or double-zeta cc-DZVP basis, respectively. The polarization of the neutral molecule with the IR field was neglected.

In order to simulate the streaking trace, 64 equally spaced pump-probe time delays were simulated with the time step of 400 as. Twelve orientations of ethyl iodide were used to mimic the random orientation of the molecule in the gas phase experiment. The orientations sample the surface of the sphere evenly.

At each XUV-pulse central frequency, the final result of the simulation is a streaking trace. In order to simulate the detector used in the experiment, only trajectories in a detection cone of 23 degrees half-opening angle around the polarization axis were taken into account. In order to analyze the streaking traces and calculate the streaking delay the same procedure that is used in case experimental data analysis is adapted. The standard deviation is estimated by splitting all trajectories that end up in the detection cone randomly into 10 different ensembles, calculating the delays with the above described procedure separately for each ensemble, and then computing the statistical spread of the results. The analysis is done separately for the two detection cones in opposite directions along the polarization axis and the final streaking delays are obtained by averaging the two results.

Calculation of the Coulomb-laser coupling (CLC) term:

The CLC corrections are calculated using the analytical formula given in eq. (4.18) in Ref.¹⁴. Here, the ionization potentials considered for ethyl iodide, atomic iodine and neon are 55.5 eV, 57.1 eV and 21.6 eV respectively.

QST calculations:

Formally, the photoemission and molecular-orientation-resolved one-photon photoionization delay $\tau_{1h\nu}(E, \hat{k}, \hat{R})$ is defined as the energy-derivative of the phase of the photoionization matrix element $I_{i,f}$ (atomic units are employed):

$$\tau_{1h\nu}(E, \hat{k}, \hat{R}) = \frac{\partial}{\partial E} \arg(I_{i,f}), \quad (\text{M3})$$

where \hat{k} denotes the photoemission direction in the molecular frame (MF) and \hat{R} is a collective variable for the Euler angles that are used to transform the description of electron dynamics from molecular frame to laboratory frame (LF). The definition of the length-gauge photoionization matrix element $I_{i,f}$ is provided in Eq. (9.3) of Ref.⁴². This quantity is calculated

within a single-center-expansion approach employing partial waves that are the energy-normalized solutions of the Lippmann-Schwinger equation defined in Ref. ⁴³. The scattering calculations were performed using the program code ePolyScat ^{44,45}. The HF wavefunction approximating the initial state of ethyl iodide was calculated employing an all-electron 6-311G**-Pople basis set for all atoms on the basis of an equilibrium geometry determined with the second-order Møller-Plesset perturbation theory. The partial-wave-expansion has been truncated at a maximum partial-wave number $l_{\max} = 50$.

The expression for $\tau_{1hv}(E, \hat{k}, \hat{R})$ in terms of the photoionization partial-wave matrix elements $I_{lm\mu}$ reads:

$$\tau_{1hv}(E, \hat{k}, \hat{R}) = \frac{\partial}{\partial E} \text{arg} \sum_{lm\mu} I_{lm\mu} Y_{lm}(\hat{k}) D_{\mu m_p}^1(\hat{R}), \quad (\text{M4})$$

where $Y_{lm}(\hat{k})$ is a spherical-harmonic function and $D_{\mu m_p}^1$ denotes a Wigner-D-matrix. The subscript m_p specifies the laser polarization direction in the LF. For the case of linear polarization considered here, $m_p = 0$. In order to obtain the photoionization delay averaged over all photoemission-angles and molecular orientations, the angle-resolved delays are weighted by a factor proportional to the partial scattering cross-section in the particular direction and summed³⁰:

$$\tau_{1hv} = \frac{1}{8\pi^2} \int d\hat{R} \int d\hat{k} \frac{|\sum_{lm\mu} I_{lm\mu} Y_{lm}(\hat{k}) D_{\mu m_p}^1(\hat{R})|^2}{\sum_{lm\mu} |I_{lm\mu}|^2} \frac{\partial}{\partial E} \text{arg} \sum_{lm\mu} I_{lm\mu} Y_{lm}(\hat{k}) D_{\mu m_p}^1(\hat{R}), \quad (\text{M5})$$

The integration over the two photoemission polar angles $\hat{k} = (\theta, \phi)$ and the Euler angles has been performed by discretizing the integrand on two Lebedev quadrature grids of order 15 (86 points).

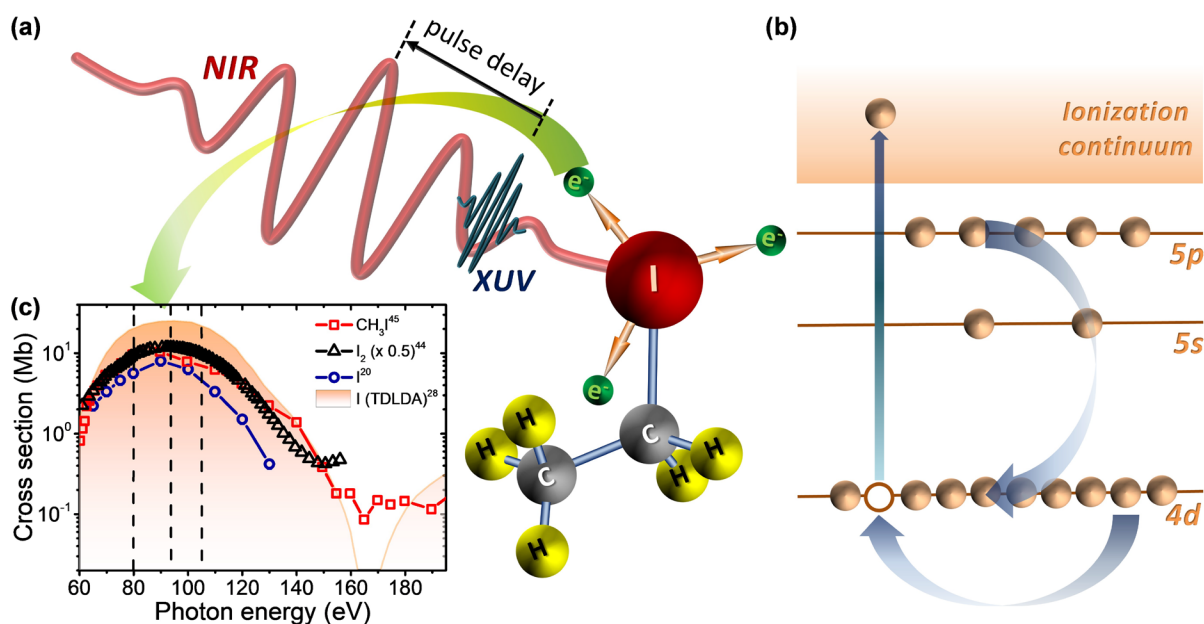


Figure 1: Photoemission delays around the giant 4d resonance in ethyl iodide. (a) Few-cycle near infrared (NIR) and isolated extreme ultraviolet (XUV) attosecond pulses with variable delay are focused onto the target jet containing neon atoms and ethyl iodide molecules. Photoelectrons, emitted in a linear photoionization process from XUV photons, are propagated in the respective atomic and molecular orbitals in the presence of the NIR laser field. The delay-dependent final streaked photoelectron energies are analysed by a time-of-flight (TOF) detector, yielding the photoelectron streaking spectrogram. For ethyl iodide, the ionized 4d electrons sample the molecular environment during their propagation. (b) The energy level diagram depicts the scheme of the photoionization process, where an electron from the 4d subshell of iodine atom within ethyl iodide is emitted into the continuum. Intra- and intershell couplings of photoelectrons, resulting in the giant dipole resonance, are illustrated by the curved arrows. (c) Photoionization cross sections for atomic iodine calculated with TDLDA³¹ (orange shaded region) together with experimentally obtained photoionization cross sections for different iodine containing compounds, including atomic²³ (blue circles) and molecular⁴⁶ iodine (black triangles) and methyl iodide⁴⁷ (red squares). The photoionization delays are analysed at different XUV photon energies, indicated by vertical dashed lines at 80, 93 and 105 eV.

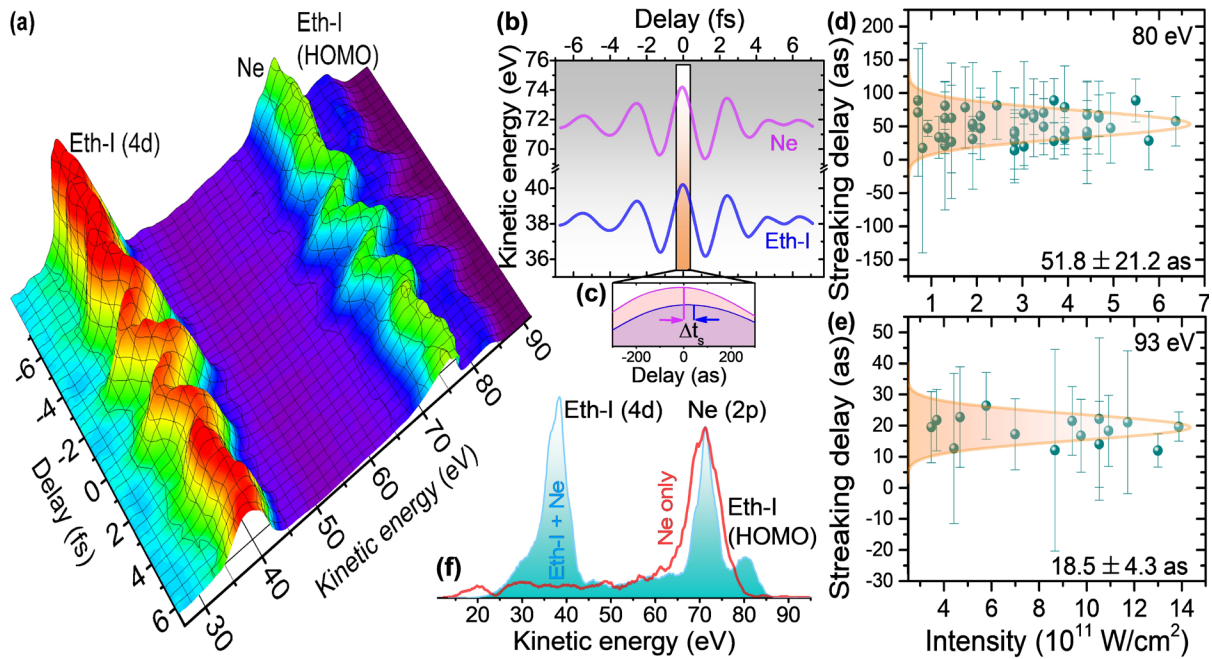


Figure 2: Ethyl iodide and neon streaking measurements. (a) Attosecond streaking spectrograms measured for neon and ethyl iodide for a photon energy centred at 93 eV. (b) Streaking traces obtained from the spectrograms by machine learning analysis, followed by Fourier filtering. (c) Enlarged view of the streaking time shift between the neon 2p and ethyl iodide 4d photoionization. (d) and (e) Relative streaking delays between neon 2p and ethyl iodide 4d from different measurements at 80 eV and 93 eV, respectively, as a function of NIR intensity calculated from the amplitude of the corresponding streaking curves. Gaussian fit (shaded area) to the streaking delay distributions yield mean values and standard deviations of (51.8 ± 21.2) as and (18.5 ± 4.3) as, respectively. (f) Normalized XUV only (no NIR) photoelectron spectra for ethyl iodide with neon (shaded area) and neon only (red curve), evidencing negligible contribution of neon 2s photoelectrons.

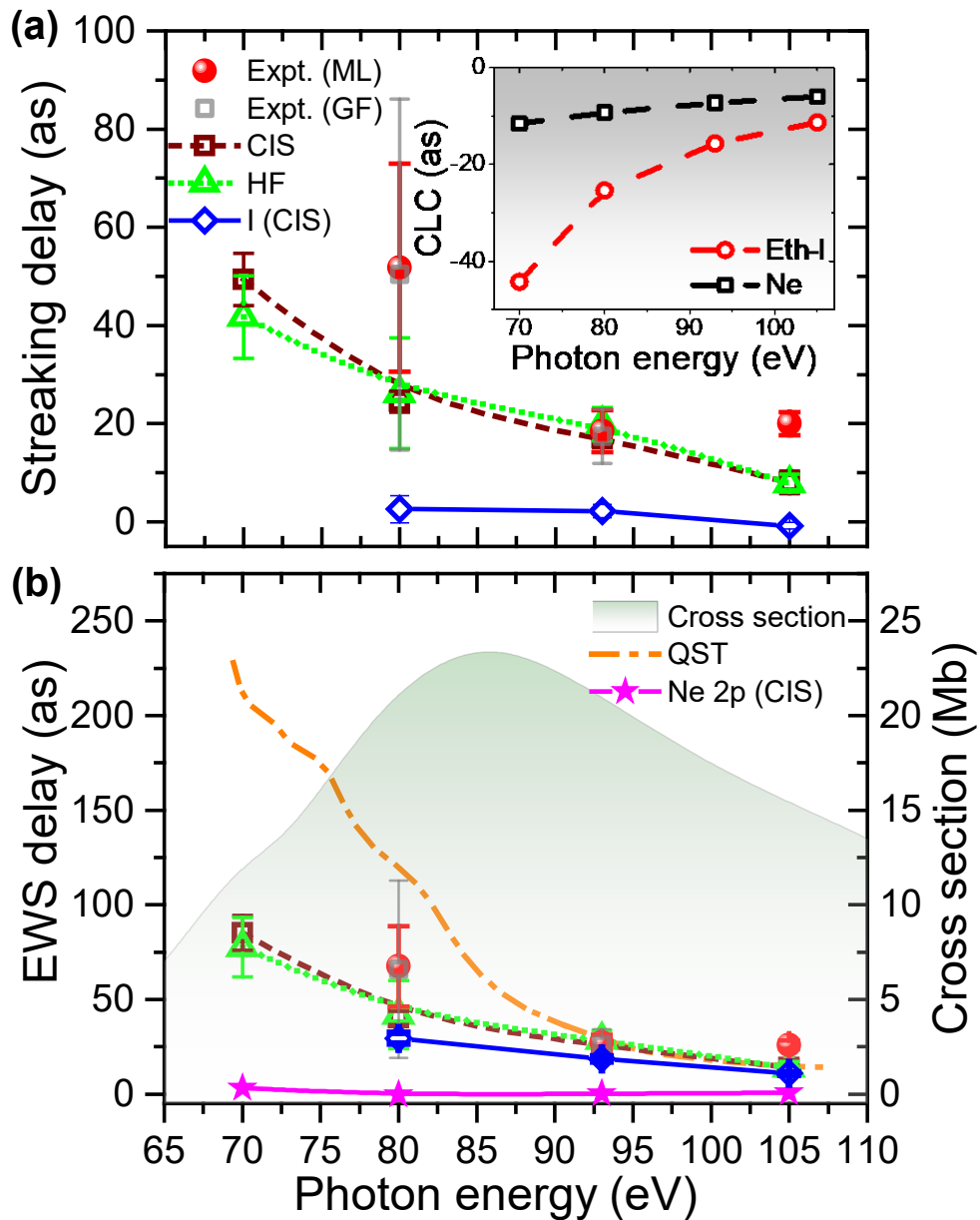


Figure 3: Streaking and EWS photoemission delays. (a) Streaking delay for ethyl iodide 4d emission relative to neon 2p emission as a function of photon energy. The red dots represent the results from the machine learning (ML) analysis, whereas the grey squares represent results from analysis using Gaussian fitting (GF). The square and triangle symbols correspond to the Classical Wigner Propagation (CWP) approach using configuration interaction singles (CIS) and Hartree-Fock (HF) formalisms, respectively. The diamond symbols represent the CIS results for atomic iodine. Inset: The CLC contributions for neon and ethyl iodide are calculated according to Ref. ¹⁴. The delay at 105 eV is extracted from Ref. ²⁶. (b) Comparison of EWS delay between different theoretical calculations and experimental data. The theory includes the quantum scattering (QST) calculation and Wigner approaches using HF and CIS for ethyl iodide. To determine absolute EWS delays from relative streaking delays for the experimental data and the CWP results, the neon 2p EWS delays calculated using the CIS model (purple stars) are added after CLC correction. In the background, the photoionization cross section (calculated using TDLDA³¹) is shown, labelled on the right vertical axis.

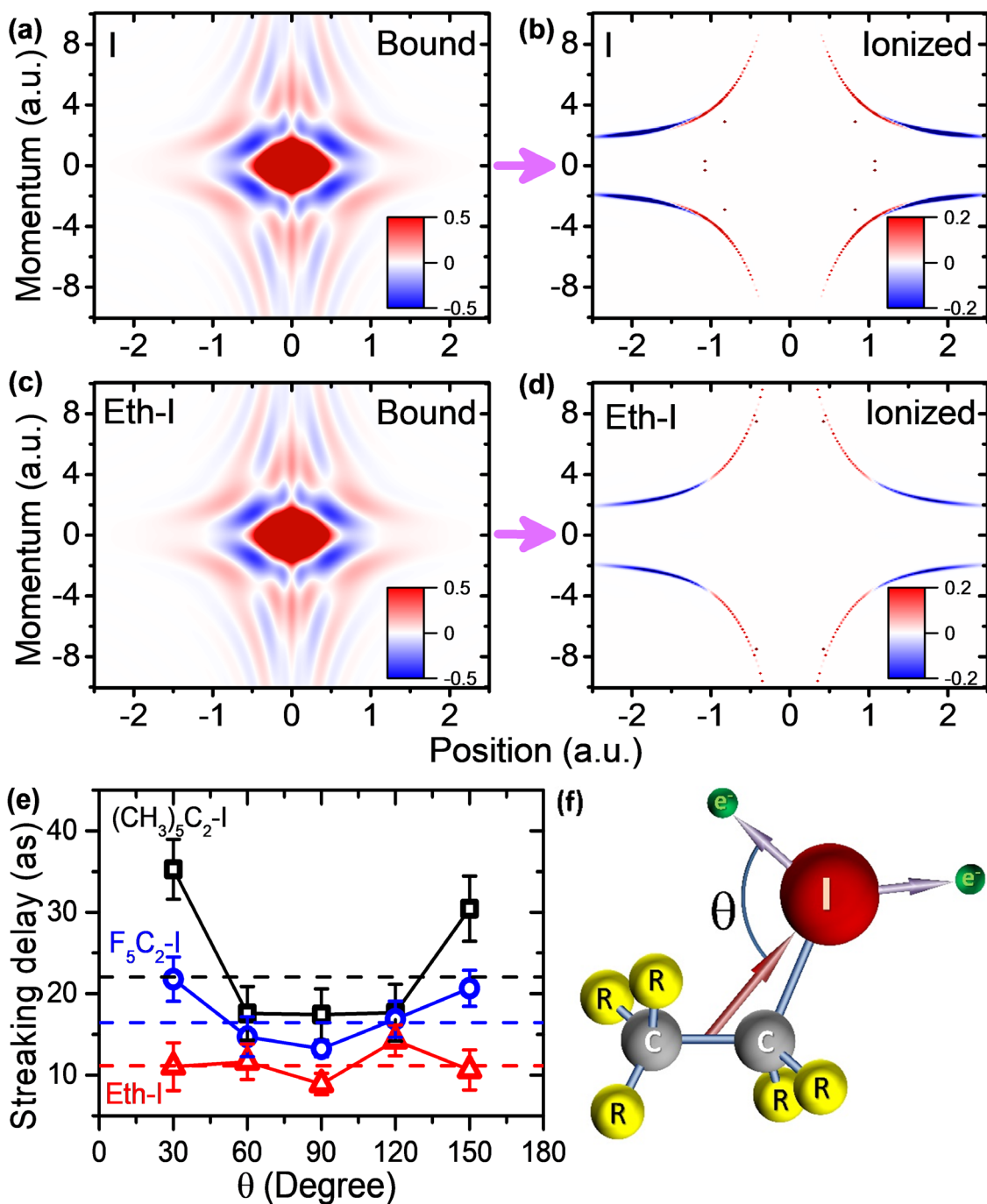


Figure 4: Comparison of the first step in the ionization process and molecular influence on photoemission delay. Wigner phase-space distribution, showing coordinate and momentum representation of an electron wavepacket, for the dipole transition from "bound" to "ionized" state of $4d \rightarrow f$ transition of the electron during the giant dipole resonance inside the iodine atom (a) and (b) and ethyl iodide (c) and (d). The "ionized" state serves as a source function providing initial conditions for classical propagation (the second step). As can be seen from the figure, the quantum-mechanically calculated first step, corresponding to transition from "bound" to "ionized" state, looks very similar for atom and molecule in the case of a giant dipole resonance. (e) Angular distribution of the streaking delay for different molecules obtained from Wigner calculations (CIS). (f) In the molecules, the angle θ is measured with respect to the line between C-C bond centre and iodine atom, shown as red arrow, where R represents either H or F or CH_3 . The angle-averaged streaking delay values are also shown as dashed horizontal lines using the same colour scheme in (e).

References:

- 1 Krausz, F. & Ivanov, M. Attosecond physics. *Rev. Mod. Phys.* **81**, 163-234 (2009).
- 2 Wigner, E. P. Lower Limit for the Energy Derivative of the Scattering Phase Shift. *Phys. Rev.* **98**, 145-147 (1955).
- 3 Cavalieri, A. L. *et al.* Attosecond spectroscopy in condensed matter. *Nature* **449**, 1029 (2007).
- 4 Ossiander, M. *et al.* Attosecond correlation dynamics. *Nat. Phys.* **13**, 280 (2016).
- 5 Schultze, M. *et al.* Delay in Photoemission. *Science* **328**, 1658-1662 (2010).
- 6 Seiffert, L. *et al.* Attosecond chronoscopy of electron scattering in dielectric nanoparticles. *Nat. Phys.* **13**, 766 (2017).
- 7 Huppert, M., Jordan, I., Baykusheva, D., von Conta, A. & Wörner, H. J. Attosecond Delays in Molecular Photoionization. *Phys. Rev. Lett.* **117**, 093001 (2016).
- 8 Isinger, M. *et al.* Photoionization in the time and frequency domain. *Science* **358**, 893-896 (2017).
- 9 Klünder, K. *et al.* Probing Single-Photon Ionization on the Attosecond Time Scale. *Phys. Rev. Lett.* **106**, 143002 (2011).
- 10 Tao, Z. *et al.* Direct time-domain observation of attosecond final-state lifetimes in photoemission from solids. *Science* **353**, 62-67 (2016).
- 11 Vos, J. *et al.* Orientation-dependent stereo Wigner time delay and electron localization in a small molecule. *Science* **360**, 1326-1330 (2018).
- 12 Haessler, S. *et al.* Phase-resolved attosecond near-threshold photoionization of molecular nitrogen. *Phys Rev A* **80**, 011404(R) (2009).
- 13 Dahlström, J. M., L'Huillier, A. & Maquet, A. Introduction to attosecond delays in photoionization. *J. Phys. B* **45**, 183001 (2012).
- 14 Pazourek, R., Nagele, S. & Burgdörfer, J. Attosecond chronoscopy of photoemission. *Rev. Mod. Phys.* **87**, 765-802 (2015).
- 15 Kamalov, A., Wang, A. L., Bucksbaum, P. H., Haxton, D. J. & Cryan, J. P. Electron Correlation Effects in Attosecond Photoionization of CO₂. *arXiv* **1906.10728** (2019).
- 16 *Giant Resonances in Atoms Molecules and Solids.*, Vol. Series B: Physics V (Springer, 1987).
- 17 Amusia, M. Y., Cherepkov, N. A., Chernysheva, L. V. & Manson, S. T. Photoionization of atomic iodine and its ions. *Phys Rev A* **61**, 020701(R) (2000).
- 18 Katsumi, K., Shunji, K., Yohji, A., Hiroshi, M. & Saburo, N. Photoelectron Spectra and Orbital Structures of Higher Alkyl Chlorides, Bromides, and Iodides. *Bull. Chem. Soc. Jpn.* **46**, 373-380 (1973).
- 19 Sewell, K. G. Photoionization Cross Section of Neon. *Phys. Rev.* **138**, A418-A421 (1965).
- 20 Eland, J. H. D. *et al.* Dissociation of multiply charged ICN by Coulomb explosion. *J. Chem. Phys.* **145**, 074303 (2016).
- 21 Schnorr, K. *XUV Pump-probe experiments on diatomic molecules. Tracing the dynamics of electron rearrangement and interatomic Coulombic decay.* (Springer Int. Pub., 2015).
- 22 Lawson, C. L. & Hanson, R. J. *Solving Least Squares Problems.* (Society for Industrial and Applied Mathematics (SIAM, 3600 Market Street, Floor 6, Philadelphia, PA 19104), 1995).
- 23 Nahon, L., Svensson, A. & Morin, P. Experimental study of the 4d ionization continuum in atomic iodine by photoelectron and photoion spectroscopy. *Phys. Rev. A* **43**, 2328-2337 (1991).
- 24 Jain, A., Gaumnitz, T., Kheifets, A. & Wörner, H. J. Using a passively stable attosecond beamline for relative photoemission time delays at high XUV photon energies. *Opt. Exp.* **26**, 28604-28620, doi:10.1364/OE.26.028604 (2018).
- 25 Zimmermann, T., Ortmann, L., Hofmann, C., Rost, J. M. & Landsman, A. S. Attosecond streaking delays in multi-electron systems. *arXiv:1804.09583v1* (2018).
- 26 Ossiander, M. *et al.* Absolute timing of the photoelectric effect. *Nature* **561**, 374-377 (2018).
- 27 Nagele, S. *et al.* Time-resolved photoemission by attosecond streaking: extraction of time information. *J. Phys. B* **44**, 081001 (2011).

- 28 Pazourek, R., Feist, J., Nagele, S. & Burgdörfer, J. Attosecond Streaking of Correlated Two-Electron Transitions in Helium. *Phys. Rev. Lett.* **108**, 163001 (2012).
- 29 Pazourek, R., Nagele, S. & Burgdörfer, J. Time-resolved photoemission on the attosecond scale: opportunities and challenges. *Faraday Disc.* **163**, 353-376 (2013).
- 30 Baykusheva, D. & Wörner, H. J. Theory of attosecond delays in molecular photoionization. *J. Chem. Phys.* **146**, 124306 (2017).
- 31 Pi, L.-W. & Landsman, A. Attosecond Time Delay in Photoionization of Noble-Gas and Halogen Atoms. *Appl. Sci.* **8**, 322 (2018).
- 32 Maia, M. & Himadri, C. Attosecond time delays in the valence photoionization of xenon and iodine at energies degenerate with core emissions. *J. Phys. Conf. Ser.* **875**, 022015 (2017).
- 33 Corkum, P. B. & Krausz, F. Attosecond science. *Nat. Phys.* **3**, 381 (2007).
- 34 Schötz, J. *et al.* Phase matching mechanism for isolated attosecond pulse generation in the overdriven regime. *submitted* (2019).
- 35 Rojas, R. *Neural networks : a systematic introduction.* (Springer-Verlag, Berlin, New York, 1996).
- 36 Srivastava, N., Hinton, G., Krizhevsky, A., Sutskever, I. & Salakhutdinov, R. Dropout: A Simple Way to Prevent Neural Networks from Overfitting. *J. Mach. Learn. Res.* **15**, 1929-1958 (2014).
- 37 Hartmann, N. *et al.* Attosecond time-energy structure of X-ray free-electron laser pulses. *Nature Photonics* **12**, 215, doi:10.1038/s41566-018-0107-6 (2018).
- 38 Patchkovskii, S., Zhao, Z., Brabec, T. & Villeneuve, D. M. High Harmonic Generation and Molecular Orbital Tomography in Multielectron Systems: Beyond the Single Active Electron Approximation. *Phys. Rev. Lett.* **97**, 123003 (2006).
- 39 Schmidt, M. W. *et al.* General atomic and molecular electronic structure system. *J. Comp. Chem.* **14**, 1347-1363 (1993).
- 40 Miyoshi, E., Sakai, Y., Tanaka, K. & Masamura, M. Relativistic dsp-model core potentials for main group elements in the fourth, fifth and sixth row and their applications. *J. Mol. Struct.: THEOCHEM* **451**, 73-79 (1998).
- 41 Sekiya, M., Noro, T., Osanai, Y. & Koga, T. Contracted polarization functions for the atoms Ca, Ga-Kr, Sr, and In-Xe. *Theor. Chem. Acc.* **106**, 297-300 (2001).
- 42 Schultz, T. & Vrakking, M. *Attosecond and XUV Physics: Ultrafast Dynamics and Spectroscopy.* (Wiley-VCH, 2014).
- 43 Lucchese, R. R. & McKoy, V. Studies of differential and total photoionization cross sections of carbon dioxide. *Phys. Rev. A* **26**, 1406-1418 (1982).
- 44 Natalense, A. P. P. & Lucchese, R. R. Cross section and asymmetry parameter calculation for sulfur 1s photoionization of SF₆. *J. Chem. Phys.* **111**, 5344-5348 (1999).
- 45 Gianturco, F. A., Lucchese, R. R. & Sanna, N. Calculation of low-energy elastic cross sections for electron-CF₄ scattering. *J. Chem. Phys.* **100**, 6464-6471 (1994).
- 46 Comes, F. J., Nielsen, U. & Schwarz, W. H. E. Inner electron excitation of iodine in the gaseous and solid phase. *J. Chem. Phys.* **58**, 2230-2237 (1973).
- 47 Lindle, D. W. *et al.* Inner-shell photoemission from the iodine atom in CH₃I. *Phys. Rev. A* **30**, 239-244 (1984).